Homopolar Bearingless Slice Motors Driving Reluctance Rotors

Minkyun Noh[a], Wolfgang Gruber[b], Jeff Speakman[c], Mark J. Gartner[c], David L. Trumper[a]

[a]Massachusetts Institute of Technology, 77 Massachusetts Avenue, Cambridge, MA 02139, USA, minkyun@mit.edu
[b]Johannes Kepler University Linz, Altenberger Straße 69, 4040 Linz, Austria
[c]Ension, Inc., 508 Pittsburgh Road, Butler, PA 16002, USA

***Abstract*—We present a bearingless slice motor that levitates and rotates a magnet-free solid-steel reluctance rotor. The motor stator uses permanent-magnet arrays near the tips of the stator teeth to provide the rotor with a homopolar bias flux. The magnet arrays are in a Halbach configuration to improve the rotor passive stiffness. The reluctance rotor has two radial fins, at the top and bottom surfaces, through which the bias flux from the magnet arrays enters. The homopolar bias flux exits the rotor via four salient rotor teeth located between the rotor radial fins. The bias flux passively stabilizes the rotor in the axial translation and in the out-of-plane tilts. The two radial translations are actively stabilized via feedback control. The stator winding consists of two sets of three-phase windings. One set of windings generates two-pole magnetomotive force (MMF) for levitation control, and the other set of windings generates eight-pole MMF for rotation control. Finite element analyses are performed to compute the performance estimates, and a prototype system is built and tested for the take-off, levitation, and rotation capabilities.**

I. Introduction

Bearingless motors are special types of electric machines in which a rotor is magnetically levitated and rotated by a single stator unit. Such magnetic levitation eliminates the need for mechanical elements such as bearings, shafts, and seals [1], and enables contact- and contamination-free operations. These characteristics make bearingless motors advantageous for special pump applications, e.g. those for blood and high-purity chemical processes. Bearingless slice motors are particularly suitable for these applications [2], [3] since they stabilize the pump impeller passively in the axial translation and out-of-plane tilts, and therefore reduce the required number of sensors and power electronics. There have been research efforts to develop bearingless slice motors driving magnet-free rotors, with a motivation for reducing the rotor cost and improving the rotor robustness. Gruber *et al.* developed a homopolar bearingless slice motor driving a reluctance rotor [4], and Noh *et al.* developed a homopolar bearingless slice motor driving a hysteresis rotor [5]. The stators of these motors have an axially magnetized permanent magnet at the stator center for homopolar flux biasing. Shinshi *et al.* developed a homopolar bearingless slice motor driving a solid-iron rotor [6]. Here, two axially magnetized permanent-magnet rings and iron rings are placed on the stator teeth for flux biasing, and the rotor has eight salient teeth.

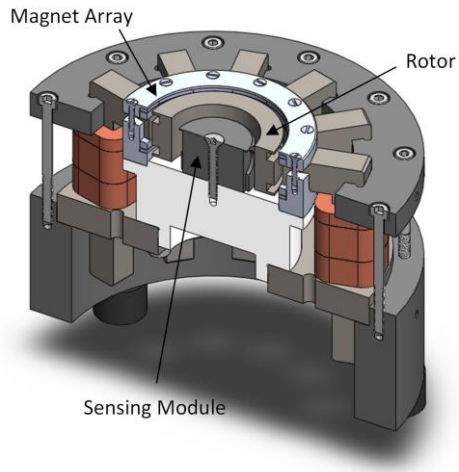

Figure 1. CAD model of our bearingless motor (cross-section view).

We have designed a new type of bearingless slice motor that levitates and rotates a magnet-free reluctance rotor, or a solid-steel rotor with saliency on the surface. The rotor is made of low-carbon solid steel. The stator has permanent magnet arrays in a Halbach configuration on the stator teeth, which provides the rotor with a homopolar bias flux. This new biasing scheme enables a single-sided magnetic design where bias flux and control flux exist on the outer rotor surface. Also, the Halbach magnet array reduces the leakage flux and improves the passive stiffness of the rotor suspension. The torque generation mechanism of our bearingless motor is similar to that of eight-pole, or four-pole-pair (p = 4), synchronous machines.

II. Bearingless Motor Design

The cross-section view of our bearingless motor is shown in Fig. 1. The motor stator consists of a temple-shape iron core, multiple concentrated coils, and magnet arrays. At the center of the stator, there is an aluminum structure against which the stator core and magnet arrays are assembled. The stator core has an annular bore to accommodate a rotor. At the center of the bore, there is a low-cost eddy-current sensing module that measures the rotor radial position, which has been used in our previous bearingless motor [7].

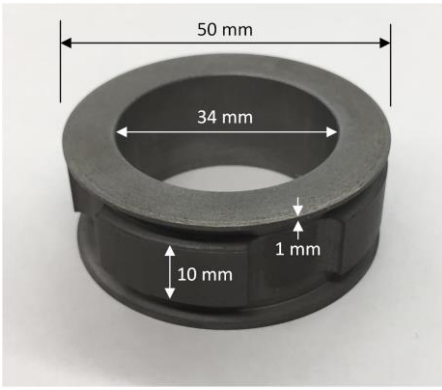

Figure 2. Solid-steel reluctance rotor.

A. Stator Core and Winding

The stator core consists of a bottom plate and twelve inverted L-shaped teeth, which form a temple architecture [2]. The pole-face area of the stator teeth is 10 mm × 10 mm. The stator teeth are circularly distributed on the stator bottom, such that the pole faces of the teeth form a bore whose diameter is 54 mm. The stator teeth and bottom plate are made of lamination-steel stacks machined via wire-EDM.

The stator winding consists of 36 concentrated coils. The coils are connected to form two sets of three-phase windings – 24 coils in the top and middle layers form a suspension winding generating a two-pole MMF, and the 12 coils in the bottom layer form a motor winding generating eight-pole MMF. The coils are made of AWG #21 magnet wire. The coils in the top layer have number of turns N_{s1} = 52, the coils in the middle layer have number of turns N_{s2} = 140, and the coils in the bottom layer have number of turns N_r = 108.

B. Magnet Arrays

Arrays of permanent magnets are located on the top and bottom of the tips of the stator teeth in order to provide a homopolar bias flux to the rotor. The magnets are arranged in a Halbach configuration along the rotor circumference, as shown in Fig. 3. That is, the magnets near the stator teeth are axially magnetized, and the other magnets farther from the stator teeth are radially magnetized toward the rotor. This magnet configuration pushes the bias flux radially inward, and therefore improves magnet utilization and the passive stiffness. Table I shows the passive stiffness on the rotor from finite element analysis (FEA) simulation using ANSYS Maxwell. The ratio between the radial stiffness k_r and axial stiffness k_z is $|k_r/k_z|$ = 1.7, which is relatively low in comparison with other bearingless motors that drive rotors consisting of permanent magnets [8]. The lower the stiffness ratio is, the easier the suspension control is for the same axial bearing performance.

TABLE I. PASSIVE STIFFNESS FROM FEA SIMULATION

	Parameter	Value
k_r	Radial Stiffness	-26.6 N/mm
k_z	Axial Stiffness	15.3 N/mm
k_ϑ	Tilting Stiffness	34.4 mNm/deg
$\|k_r/k_z\|$	Stiffness Ratio	1.7

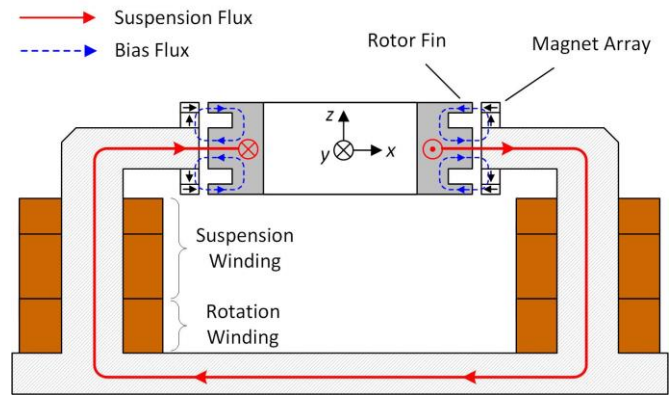

Figure 3. Schematic diagram showing the Halbach-type magnet arrays providing the rotor with homopolar bias flux (dashed blue line). The stator can generate a suspension force by superimposing two-pole suspension flux (solid red line)

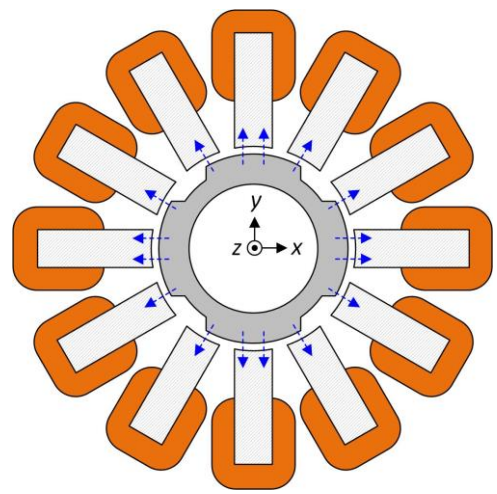

Figure 4. Schematic diagram showing the bias flux (dashed blue line) in the airgap. The rotor saliency modulates the bias flux such that the flux density is high on the rotor teeth and low on the rotor slots.

Two types of arc-shape NdFeB magnets (grade N35) are used to construct the magnet arrays. One type is axially magnetized and the other type is radially magnetized, and both types have the same geometry; the thickness of the arc is 1.5 mm, the width is 3 mm, and the arc angle is 30°. The array closer to the stator teeth consists of 24 axially magnetized magnets in two layers, and the array far from the stator teeth consists of 12 radially magnetized magnets in a single layer. That is, the axially magnetized array is twice as thick as the radially magnetized array.

C. Reluctance Rotor

The rotor is made of low-carbon solid steel (AISI 1018). Fig. 2 shows the reluctance rotor of our bearingless motor. The rotor is 50 mm in outer diameter and 34 mm in inner diameter. The rotor has two radial fins of 1 mm thickness at the top and bottom of the rotor. The rotor has four teeth evenly displaced along the circumference and between the radial fins. The thickness of the rotor teeth is 10 mm, which matches the thickness of the stator teeth. The bias flux from the magnet array enters the rotor through the radial fins and exits from the rotor teeth, as shown in Fig. 3 and Fig. 4.

III. Operating Principle

The stator windings generate MMFs that interact with the air-gap bias flux, thereby generating suspension forces and driving torque.

The suspension winding generates a two-pole MMF around the rotor, which causes imbalance of the flux density in the air-gap and therefore generates a reluctance force. Fig. 3 illustrates the operating principle of the suspension. Here, the dashed blue lines denote the homopolar bias flux from the magnet arrays, and the solid red lines denote the two-pole suspension flux induced by the suspension winding MMF. In this figure, the suspension flux strengthens the bias flux on the right and weakens it on the left, and therefore generates a net radial force. The direction and magnitude of the suspension winding MMF can be controlled based on the measured rotor position such that the rotor is centered on the stator. The operating principle for suspension is similar to that of [5], except that in our new motor the bias flux exists in the outer air-gap only.

The rotor teeth modulate the air-gap bias flux as in Fig. 4; the flux is more concentrated on the rotor teeth than the slots. This flux distribution can be conceptually decomposed into homopolar and eight-pole heteropolar components. The torque is generated when the rotation winding applies an eight-pole MMF so as to interact with the eight-pole component of the bias flux in synchronism. The resulting torque generation principle is similar to that of synchronous machines.

IV. Prototype System

We have built a prototype system as shown in Fig. 5. The bearingless motor forms a closed-loop system with a peripheral devices such as sensing module, real-time computers, and power amplifiers. The block diagram in Fig. 6 shows the system composition in details.

The rotation control system consists of Hall-effect sensors (SS49E, Honeywell), cRIO real-time computer (cRIO-9064, National Instruments), three-phase power amplifier (LA-210T, Varedan), and the rotation winding of the bearingless motor. The Hall sensors are inserted in the stator slots to measure the air-gap flux density, thereby estimating the rotor angle and speed. The angle and speed estimates are fed back to the real-time computer for feedback control. The power amplifier is configured for a transconductance ratio 1 A/V and a bandwidth of about 900 Hz.

The suspension control system consists of a low-cost eddy-current sensing module [7], cRIO real-time computer (cRIO-9064, National Instruments), three-phase trans-conductance amplifier (LA-210T, Varedan), and three-phase suspension winding. The sensing module measures the radial positions $\hat{x}$ and $\hat{y}$ of the rotor and sends them to the real-time computer for feedback control. The power amplifier is configured for a transconductance ratio 1 A/V and a bandwidth about 5.5 kHz.

The eddy-current sensing module consists of sensing coils (WR111180-36F5-B1, TDK Corporation), Inductance to Digital converters (LDC 1101, Texas Instruments), and myRIO real-time computer (myRIO-1900, National Instruments). The sensing coils form LC oscillators with the capacitors on the LDC boards, and the LDCs drive the oscillators at their resonance frequencies (2.4-3.3 MHz). The high frequency magnetic fields generated from the coils

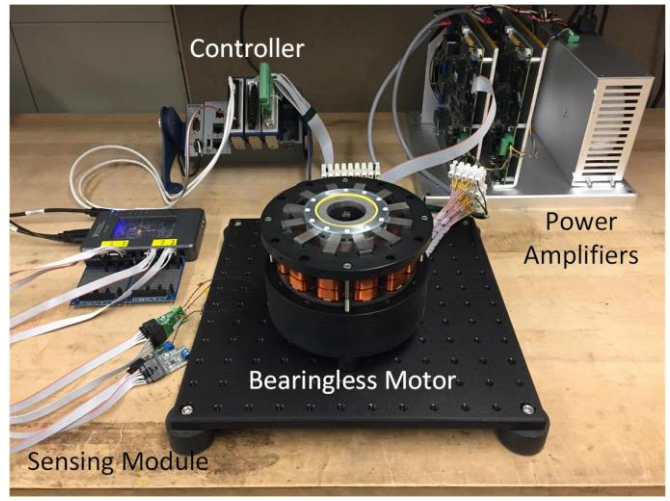

Figure 5. Photograph of the prototype system.

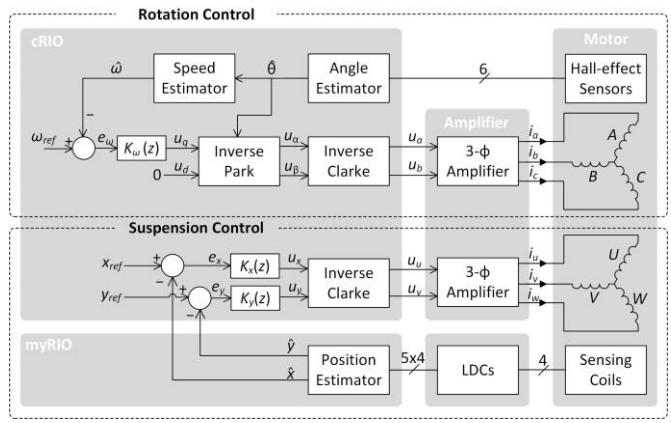

Figure 6. Block diagram of the control system.

induce eddy currents on the rotor inner surface, which change the resonance frequencies of the sensing coils as a function of the rotor position. The LDCs count the number of oscillations during a specified time window, e.g., T_s = 500 μs, and send these values to the myRIO real-time computer via SPI communication. The myRIO computes the rotor position estimates $\hat{x}$ and $\hat{y}$ and sends them to the cRIO real-time computer via analog output channels. The details of the position measurement using LDCs are presented in [7].

Table II shows the performance estimates from FEA simulation using ANSYS Maxwell.

TABLE II. Performance Estimates from FEA Simulation

	Parameter	Value
K_τ	Torque Constant	31 mNm/A_{rms}
I_o	Rated Current	1.3 A_{rms} (3.2 A_{rms}/mm^2)
τ_o	Rated Torque	40.3 mNm

V. Control

In our bearingless motor, the mechanisms for suspension force generation and driving torque generation are decoupled in the hardware. This is a common characteristic of homopolar

bearingless motors [5]. Therefore, as shown in the block diagram in Fig. 6, the controllers are implemented separately for the rotation and suspension control loops.

A. Suspension Control

The suspension control is implemented in the field-programmable gate array (FPGA) of the cRIO computer. Two discrete-time lead controllers $K_x(z)$ and $K_y(z)$ are implemented for x- and y-axes suspension control, followed by Inverse Clark transformation that transforms control signals from the two-phase coordinate to the three-phase coordinate. The loop rate of the suspension control is synchronized to the update rate f_s = 2 kHz of the eddy-current sensing module.

The rotor radial position is open-loop unstable due to the negative stiffness arising from the bias flux, and the suspension controller stabilizes it via feedback control. Specifically, the controllers $K_x(z)$ and $K_y(z)$ process the position error signals $e_x = x_{ref} - \hat{x}$ and $e_y = y_{ref} - \hat{y}$ to generate control signals u_x and u_y. The control signals u_x and u_y are transformed to u_u and u_v via Inverse Clarke transformation, and sent to the three-phase transconductance amplifier as the reference signals for the currents i_u and i_v through phase U and V, respectively. Due to the star-connection of the three phases, the current i_w through phase W is constrained such that $i_w + i_u + i_v = 0$.

B. Rotation Control

The rotation control is implemented in the cRIO computer; a discrete-time PI controller $K_\omega(z)$ is implemented in the real-time processor at 1 kHz, and estimation and transformation algorithms are implemented in the FPGA at 10 kHz.

The speed controller regulates the rotational speed of the motor around the reference value. Specifically, the speed controller $K_\omega(z)$ takes the speed error $e_\omega = \omega_{ref} - \hat{\omega}$ and computes the control signal u_q. A series of coordinate transformations allow the control signal u_q to determine the q-axis current i_q, and therefore the motor torque. First, the rotor angle is estimated based on the Hall sensor measurements. Then, the angle estimate is used in an Inverse Park transformation to change the coordinates of the control signals from the rotational dq-coordinate to the stationary $\alpha\beta$-coordinate. This is followed by an Inverse Clarke transformation to compute the control signals in the three-phase stationary abc-coordinate, which are then sent to the three-phase transconductance amplifiers.

VI. Test Results

We have tested the takeoff, levitation, and rotation capabilities of the prototype bearingless motor.

A. Suspension Test

The magnetic gap, or the distance between the stator bore and the rotor outer surface when the rotor is centered, is 2 mm. Plastic shims are inserted into the magnetic gap such that the rotor is off-centered by 0.5 mm when the rotor touches the wall. As we turn on the suspension controller, the rotor takes off from the wall and levitates at the stator center. Fig. 7 shows the step response of the x-axis suspension. Here, we apply a step reference signal whose peak-to-peak amplitude is 0.04 V (33 μm). The overshoot is about 55%, which corresponds to a phase margin estimate of φ_m = 18° via $\zeta \approx \varphi_m/100$. The rise time is about t_r = 3-4 ms, which corresponds to a bandwidth estimate of f_h = 82-110 Hz, via $t_r \approx 2.2/\omega_h$, where $\omega_h = 2\pi f_h$.

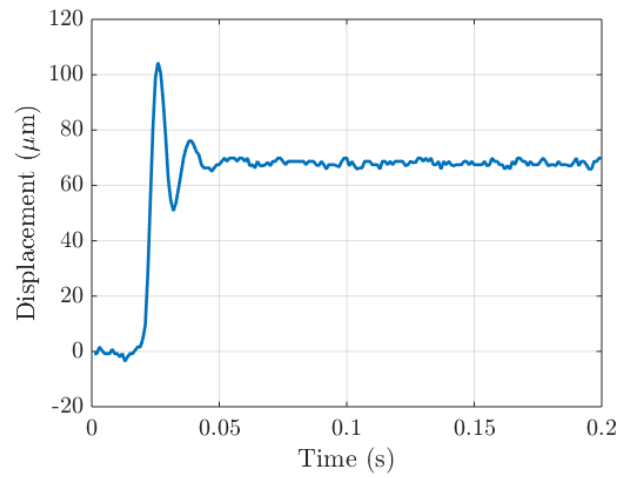

Figure 7. Step response of the x-axis suspension.

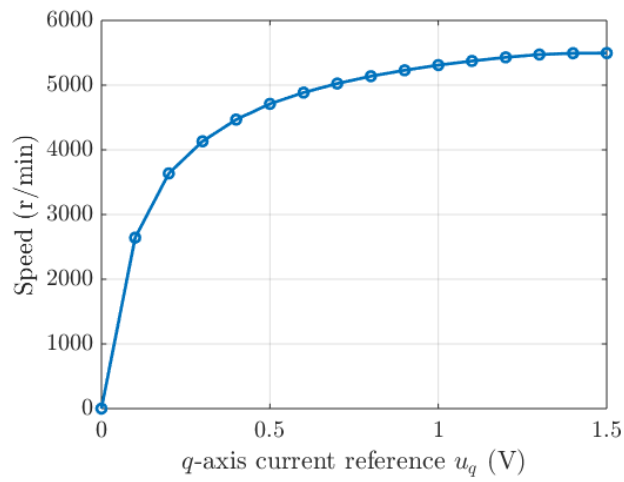

Figure 8. Open-loop steady-state rotor speeds as limited by an air drag.

B. Rotation Test

We have measured the open-loop steady-state rotor speeds of our bearingless motor. The steady-state is reached due to the air-drag torque. The control signal u_q is incremented from 0 V to 1.5 V, which maps to the q-axis current i_q from 0 A to 1.5 A unless the transconductance amplifier saturates in voltage. Fig. 8 shows the relation between the control signal u_q and the open-loop steady-state rotor speed. The maximum no-load speed of our motor is about 5500 r/min, beyond which the speed exhibits saturation. We postulate that this speed limit is due to the amplifier saturation, which is caused by the relatively low bus voltage (± 60 V) and relatively large phase-to-phase inductance (37 mH) of the rotation winding.

VII. Conclusion

In this paper, we have presented a new bearingless motor that levitates and rotates a magnet-free solid-steel rotor. The elimination of permanent magnets from the moving part makes this motor suitable for special applications, such as

blood pumps with disposable impeller modules. We have built a prototype system, and demonstrated the feasibility of our new motor design via levitation and rotation tests. We next plan to implement pumping tests with water and blood.

ACKNOWLEDGEMENT

This work was supported by the National Heart, Lung, and Blood Institute of the National Institute of Health under Award R41HL134455. The content is solely the responsibility of the authors and does not necessarily represent the official views of the National Institutes of Health.

The work of M. Noh was partially supported by the Samsung Scholarship.

The authors thank Fred Sommerhalter for fabricating the stator coils, and thank Christian Baumschlager at WIHO Hofbauer GmbH for fabricating the stator cores.

REFERENCES

[1] A. Chiba, T. Fukao, O. Ichikawa, M. Oshima, M. Takemotor, and D. G. Dorrell, *Magnetic Bearings and Bearingless Drives*. Amsterdam, The Netherlands: Elsevier-Newnes, 2005.

[2] N. Barletta and R. Schöb, "Design of a bearingless blood pump," in *Proc. 3rd International Symposium on Magnetic Suspension Technology*, Jul. 1996, pp. 265–274.

[3] R. Schöb and N. Barletta, "Principle and application of a bearingless slice motor," in *Proc. 5th International Symposium on Magnetic Bearings*, Aug. 1996, pp. 313–318.

[4] W. Gruber, M. Rothböck, and R. Schöb, "Design of a novel homopolar bearingless slice motor with reluctance rotor," *IEEE Transactions on Industry Applications*, vol. 51, no. 2, pp. 1456–1464, Mar. 2015.

[5] M. Noh, W. Gruber, and D. L. Trumper, "Hysteresis Bearingless Slice Motors With Homopolar Flux-Biasing," *IEEE/ASME Transactions on Mechatronics*, vol. 22, no. 5, pp. 2308–2318, Oct. 2017.

[6] T. Shinshi, R. Yamamoto, Y. Nagira, and J. Asama, "A Bearingless Slice Motor with a Solid Iron Rotor for Disposable Centrifugal Blood Pump," in *Proc. Intenational Power Electronics Conference*, May 2018, pp. 4016–4019.

[7] M. Noh, W. Gruber and D. L. Trumper, "Low-cost eddy-current position sensing for bearingless motor suspension control," in *Proc. IEEE International Electric Machines and Drives Conference (IEMDC)*, 2017.

[8] P. Püntener, F. Hoffmann, D. Menzi, D. Steinert, and J. W. Kolar, "Homopolar bearingless slice motor in temple design," in *Proc. IEEE International Electric Machines and Drives Conference (IEMDC)*, 2017.